npj | flexible electronics

www.nature.com/npjflexelectron

ARTICLE OPEN

Check for updates

Flexible fully organic indirect detector for megaelectronvolts proton beams

Sabrina Calvi[1,2], Laura Basiricò[3,4]✉, Sara M. Carturan[5,6], Ilaria Fratelli[3,4], Antonio Valletta[1,2], Alberto Aloisio[7,8,9,10], Stefania De Rosa[1], Felix Pino[5,6], Marcello Campajola[8], Andrea Ciavatti[3,4], Luca Tortora[1,2,11], Matteo Rapisarda[1,2], Sandra Moretto[5,12], Matteo Verdi[3,4], Stefano Bertoldo[6], Olivia Cesarini[6], Paolo Di Meo[8], Massimo Chiari[13], Francesco Tommasino[14,15], Ettore Sarnelli[8,9], Luigi Mariucci[1,2], Paolo Branchini[1,2], Alberto Quaranta[15,16] and Beatrice Fraboni[3,4]

A flexible, fully organic detector for proton beams is presented here. The detector operates in the indirect mode and is composed of a polysiloxane-based scintillating layer coupled to an organic phototransistor, that is assessed for flexibility and low-voltage operation ($V = -1$ V), with a limit of detection of 0.026 Gy min^{-1}. We present a kinetic model able to precisely reproduce the dynamic response of the device under irradiation and to provide further insight into the physical processes controlling it. This detector is designed to target real-time and in-situ dose monitoring during proton therapy and demonstrates mechanical flexibility and low power operation, assessing its potential employment as a personal dosimeter with high comfort and low risk for the patient. The results show how such a proton detector represents a promising tool for real-time particle detection over a large area and irregular surfaces, suitable for many applications, from experimental scientific research to innovative theranostics.

npj Flexible Electronics (2023)7:5 ; https://doi.org/10.1038/s41528-022-00229-w

INTRODUCTION

The development of high-performing, thin, and flexible sensors for the detection of ionizing radiation in real-time at affordable costs is of increasing interest, as the technology currently available still fails to address the requirements of large-area, conformability and portability, lightweight, and low-power operation[1]. The fields of application range from medical diagnostics and therapy to astrophysics, high energy physics, as well as industrial testing, including civil radiation safety[2]. Up to now, the research focused greatly on X-ray detection, but the development of innovative charged particles detectors able to retain the above-described peculiarities (e.g., flexibility, scalability to large-area, and low power operation) would be particularly attractive, especially for real-time hadron therapy dosimetry. Proton therapy is currently one of the most advanced medical therapy tools for cancer treatment. Compared to X-ray therapy, where the delivered dose of radiation decreases exponentially with depth, a proton beam allows delivering a conformal radiation dose by tuning and focusing the peak of the maximum released energy (the Bragg peak) on the selected volume[3], sparing the surrounding healthy tissues. However, toxicities may still occur within or very close to the target, due to the combination of suboptimal beam arrangement, organ motion, and range uncertainty[4,5]. A real-time beam monitoring and dose-measuring by a flexible, thin, and human-tissue-equivalent detector is therefore needed to verify the actual dose delivered during the proton-therapy session to healthy tissues close to the target cancer, preventing long-term toxic effects. Current therapy treatment plans are conceived by means of sophisticated simulation codes and designed experiments on customized phantoms[6]. An experimental real-time and in situ dose monitoring during therapy, carried out by means of a thin wearable device, would be a game shifter, providing highly beneficial[7] improvements in cancer patients' care quality and precision.

Fully organic detectors are promising systems for advanced dosimetry, as their mechanical features allow devices to be adapted to complex contoured and large area surfaces, with outstanding portability and lightweight. Further, their human-tissue-equivalent properties, thanks to their density and composition, make them ideal candidates for medical dosimetry applications, as demonstrated in last years for the direct detection of ionizing radiation by organic thin films[8–13] and single crystals[14–18]. The indirect detection of ionizing radiation is another effective tool, implemented via a two-step process: (i) the conversion of ionizing radiation into visible photons, carried out by a scintillator, and (ii) the conversion of the visible photons emitted by the scintillator into an electrical signal by a properly matched photoelectric device. With respect to the direct detection approach, in the indirect detectors, a scintillation layer with a thickness ranging from 0.1 to a few mm, allows the absorption of a larger amount of energy from the impinging radiation. The possibility to improve the stopping power of the indirect detector leads to very good detection performance at high radiation energies, more challenging to detect by thin-film-based direct detectors. On the other hand, indirect detectors typically exhibit high radiation tolerance at low energies, i.e., when the whole

[1]INFN, Sezione di RomaTre, Via Della Vasca Navale 84, 00146 Roma, Italy. [2]CNR - Institute for Microelectronics and Microsystems (IMM) Via Del Fosso Del Cavaliere, 100, 00133 Rome, Italy. [3]Department of Physics and Astronomy, University of Bologna, Viale C. Berti Pichat 6/2, 40127 Bologna, Italy. [4]INFN, Sezione di Bologna, Viale C. Berti Pichat 6/2, 40127 Bologna, Italy. [5]Department of Physics and Astronomy, University of Padova, Via Marzolo 8, Padova, Italy. [6]INFN - Laboratori Nazionali di Legnaro, Viale dell'Università 2, Legnaro, Italy. [7]University of Naples Federico II, Department of Physics, Complesso Univ. di Monte S. Angelo, Edificio G, Via Cintia, 80126 Napoli, Italy. [8]INFN - Sezione di Napoli - Complesso Univ. di Monte S. Angelo, Edificio G, Via Cintia, 80126 Napoli, Italy. [9]CNR-SPIN, Via Campi Flegrei, 34, 80078 Pozzuoli, NA, Italy. [10]Task Force di Bioelettronica, University of Naples Federico II, Napoli, Italy. [11]Department of Sciences, Roma Tre University, Via della Vasca Navale 84, 00146 Roma, Italy. [12]INFN, Sezione di Padova, Via Marzolo 8, Padova, Italy. [13]INFN, Sezione di Firenze, Via G. Sansone 1, 50019 Sesto Fiorentino, Florence, Italy. [14]Department of Physics, University of Trento, Via Sommarive 14, 38123 Trento, Povo, Italy. [15]INFN-TIFPA, Via Sommarive 14, 38123 Trento, Povo, Italy. [16]Department of Industrial Engineering, University of Trento, Via Sommarive 9, 38123 Trento, Povo, Italy. ✉email: laura.basirico2@unibo.it

particle energy is released into the scintillator, thanks to the sparing of the photodetector from the impinging beam. To implement an indirect detector for ionizing radiation, the scintillation-produced UV–vis photons need to be converted into an electronic signal by a properly matched photoelectric device. This approach, applied to an organic electronic device, has been explored only for X-ray detection so far[19].

In this work, we report on a fully organic, flexible proton detector operating in the indirect mode based on the combination of a polysiloxane-based flexible scintillator with a flexible organic phototransistor (OPT). Polysiloxane-based scintillators are intrinsically flexible, are highly resistant to gamma-ray and ion irradiation[20,21], to high temperatures, to moisture and organic solvents besides offering optimal light output, with discrimination capabilities between different types of ionizing radiation[22]. These characteristics make them more suitable than commercial plastic scintillators and inorganic rigid crystals[23] for applications involving radiation monitoring in contact with human tissues or in complex environments. Besides, OPTs combine high sensitivity with intrinsic signal amplification limiting noise issues to a simplified external circuitry. Preliminary reports in the early 2000s on organic UV-vis photodetector for indirect ionizing radiation detection[24,25] lead to recent results on organic photodiodes in X-rays image sensor arrays[26] on flexible plastic substrates[27], working at low voltages (−1 V) and targeting dosimetry for medical application. An OPT active matrix has been proposed for indirect X-ray imaging application and the first indirect X-ray detector, based on OPT arrays coupled with an organic scintillation layer, was only recently reported[28].

Here, we demonstrate the suitability of a flexible organic detector based, on the coupling of polysiloxane scintillators with OPT fabricated on thin plastic foil, for the real-time monitoring of low energy (5 MeV) proton beams. The detector has been assessed for flexibility and operation at low power supply, assuring high comfort and low electric risk for its employment as a personal dosimeter. Further, we present a kinetic model, developed to describe the detector response mechanism, able to precisely reproduce the dynamic response of the device under proton irradiation and to provide further insight into the physical processes controlling its response.

RESULTS

Fully organic indirect detector configuration

The schematic cross-section of the here presented fully organic indirect radiation detector is shown in Fig. 1a, and optical images are shown in Fig. 1b. First, the OPT, based on dinaphtho[2,3-b:2′,3′-f]thieno[3,2-b]thiophene (DNTT) as the active layer, was fabricated onto a 100 µm thick polyethylene-naphthalate (PEN) foil, which allows combining flexibility with a carrier-free large-area compatible process. The OPT was developed to work at the low power supply, combining high bias stress tolerance and bending stability with high sensitivity at weak light intensities at a suitable optical absorption wavelength. Then, the 500 µm thick scintillating plastic film is integrated directly on top of the passivation layer. The scintillator is synthesized using a polysiloxane-based matrix, a primary dye (2,5-diphenyl oxazole PPO), and a wavelength shifter (Lumogen Violet®). Two different matrices were considered and compared, the homopolymer polymethylphenylsiloxane (PSS100), whose response under irradiation with ions, gamma-rays, and fast neutrons has been extensively reported and commented[22], and the co-polymer, polyvinylphenyl-co-phenylmethyl siloxane (PVP-MPS), whose response as a base material for scintillators is herein reported. This matrix has a chemical structure similar to PSS100, with a monophenyl unit as a substituent on silicon, either methylphenyl or vinylphenyl, and a very close molar concentration of phenyl groups, hence high scintillation yield is expected[29]. On the other hand, in PVP-MPS the vinyl reactive groups involved in the cross-linking process are present as substituents along the chain of the base resin, as well as terminal groups, and their amount per unit volume is much higher as compared to PSS100 (Supplementary Table 2). This could enhance the density of cross-linkages and, in turn, the resistance to damage. Therefore, both formulations have been considered for the tests. Hereafter the matrix material acronym (PSS100 or PVP-MPS) is used to indicate the corresponding scintillating film.

The motivation of the work we carried out was to assess our device for the challenging application of the in-situ and real-time monitoring of the radiation dose impinging onto healthy tissues during a session of proton therapy, e.g., in prostate tumor treatment. To meaningfully address this task, we need to know with which energy range scattered protons irradiate healthy tissues. For a complete analysis of the problem, the main parameters are the dose released and the linear energy transfer (LET) distribution. A representative treatment plan for a prostate cancer patient is shown in Fig. 1c, d. The dose (Fig. 1c) was calculated with the Monte Carlo (MC) algorithm of the commercial system Raystation, while the dose-average LET (Fig. 1d and Supplementary Fig. 1a) was retrieved with a previously validated version of the TOPAS MC code[30]. The energy range of incoming protons was (162 ÷ 197) MeV, and two opposing fields were employed. The plan was calculated with a schedule of 2 Gy × 39 fractions, assuming a constant relative biological effectiveness RBE = 1.1 for protons, according to current clinical practice. Due to partial overlap with the target volume, the rectum receives medium-high doses. At the same time, the highest LET values are distributed at the edge of the target as well as in the rectum. This corresponds to low-energy protons (few MeV) characterizing the distal edge as well as the lateral penumbra of the field.

We tested the devices at the LABEC ion beam center (Laboratory of Nuclear Techniques for the Environment and Cultural Heritage, National Institute for Nuclear Physics INFN Firenze, Italy), where the above-described conditions can be reproduced (e.g., beam energy at the end of the path and deposited energy per unit volume). The final coupled full-organic indirect detectors were thus tested for responsivity, dose rate linearity and measurements repeatability using a 5 MeV beam. The proton penetration depth of 5 MeV proton beam inside the PSS100 and PVP-MPS siloxane scintillator films was calculated through the Stopping and Range of Ions in Matter (SRIM) Monte Carlo code[31], resulting in both cases below 400 µm. In Fig. 1e the simulated LET released by the 5 MeV proton beam in both materials in terms of [keV µm^{-1}] varies between 8 up to 40 keV µm^{-1}, thereby matching the LET of a therapeutic beam close to being stopped by the material (Supplementary Fig. 1a). The 5 MeV proton beam releases entirely its energy and full stops inside the 0.5 mm scintillating films (in Supplementary Fig. 2 the proton range in the two films is reported), thus maximizing the scintillation efficiency, preserving the underlying OPT from possible damage due to direct proton exposure and granting a proper assessment of the decoupled/independent response of both the scintillator and the OPT.

Figure 1f reports the variation of the detector response obtained mimicking a typical operating condition during a proton therapy session. During the test, the device is exposed to 10 s radiation cycles with different intensities, while the control measurements are collected after 28 and 50 min under a pulse with irradiance 6.5×10^7 H$^+$ s^{-1} cm^{-2}. The device operates at a very low bias voltage ($V_{ds} = V_{gs} = -1$ V), hence it is compliant with basic safety constraints for electrical hazards. The results show that the device response is reliable and stable until the end of the session and beyond.

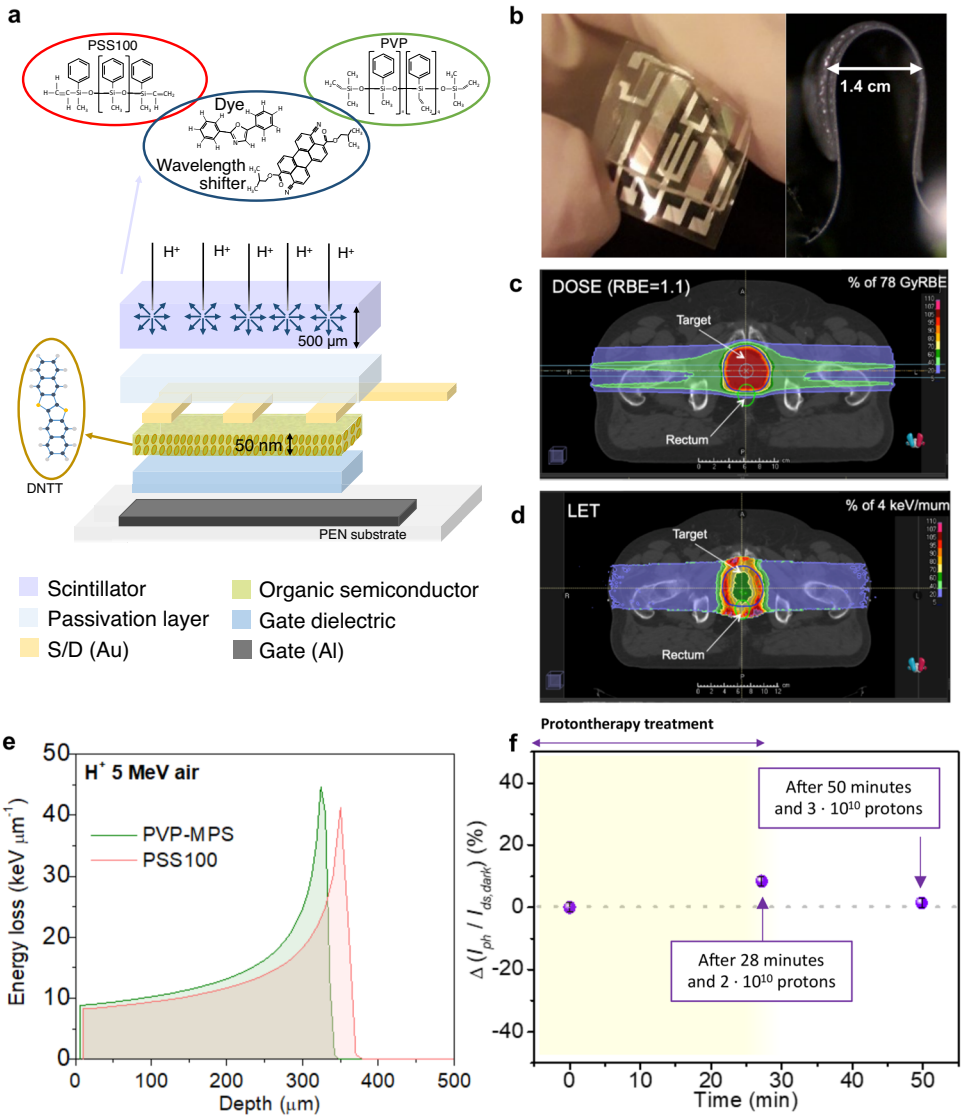

Fig. 1 Flexible fully organic indirect proton detector. a Detector cross-section scheme. The layer dimensions and relative thicknesses are out of scale. Chemical structures and thicknesses of the organic semiconductor and the scintillator layers are also indicated. **b** Flexible indirect proton detector 2 × 2 matrices. **c**, **d** Monte Carlo simulations of a single treatment run, reaching a total dose of 2 Gy on the cancer volume by protons irradiation with energy in the range (162 ÷ 197) MeV: dose distribution as % of 78 GyRBE (**c**) and dose-average LET distribution as % of 4 keV μm^{-1} (**d**). **e** Simulated curves of the energy loss of each 5 MeV proton impinging in PSS100-(red) and PVP-MPS-(green) based scintillators. The area below the curves corresponds to the total energy released inside the material. **f** Reliability of the detector response benchmarked by measuring the photocurrent signal rise upon irradiation with a fixed proton flux (i.e., 6.5×10^7 $H^+ s^{-1}$ cm^{-2}) at the beginning of the experiment, i.e., unirradiated device, and after fixed total proton irradiation (2×10^{10} H^+ and 3×10^{10} H^+). The yellowish region indicates the temporal window typical of a proton therapy run.

Scintillator performance

Two main critical features must be considered for the development of an indirect ionizing radiation detector. The first concerns the proper matching between the scintillation light wavelength and the optical absorption of the OPT active layer. The second one is to employ as OPT active layer an organic semiconductor with high field-effect mobility (μ_{FE}), which is directly proportional to the OPT responsivity[32,33]. The most suitable solutions at the state-of-the-art are summarized in Table S1. The optimal coupling between the chosen blue emitting scintillator and the air-stable, high-mobility DNTT semiconductor is shown in Fig. 2a. The ion beam-induced luminescence (IBIL) spectra of the scintillators under irradiation with 2 MeV protons and the UV–vis absorbance spectrum of the DNTT film show a good overlapping, assuring spectral matching between the light emitting sensor (siloxane) and the photoconverter (DNTT sensitized OPT).

The herein-used PSS100 and PVP-MPS-based scintillating films present an optimal combination of mechanical and optical properties, which make them suitable candidates to be coupled with a light detector fabricated onto a flexible substrate. The elastomeric nature of polysiloxanes is well known, having glass transition temperature well below room temperature (−125 ÷ −90) °C. They are soft and pliable, with an elongation at break in the range (100 ÷ 500) % tensile strength around (5 ÷ 10) MPa and Young modulus variable between 1 MPa and 3 MPa, although the presence of phenyl side groups might affect these features[34]. It is evident that well-performing plastic commercial scintillators (e.g., EJ-212) have much more limited flexibility, due to their rigid base polymers, i.e., polystyrene or polyvinyltoluene (Fig. 2b).

Figure 2c reports the pulse height spectra of 0.5 mm thick samples of PSS100 and PVP-MPS scintillators exposed to ^{241}Am

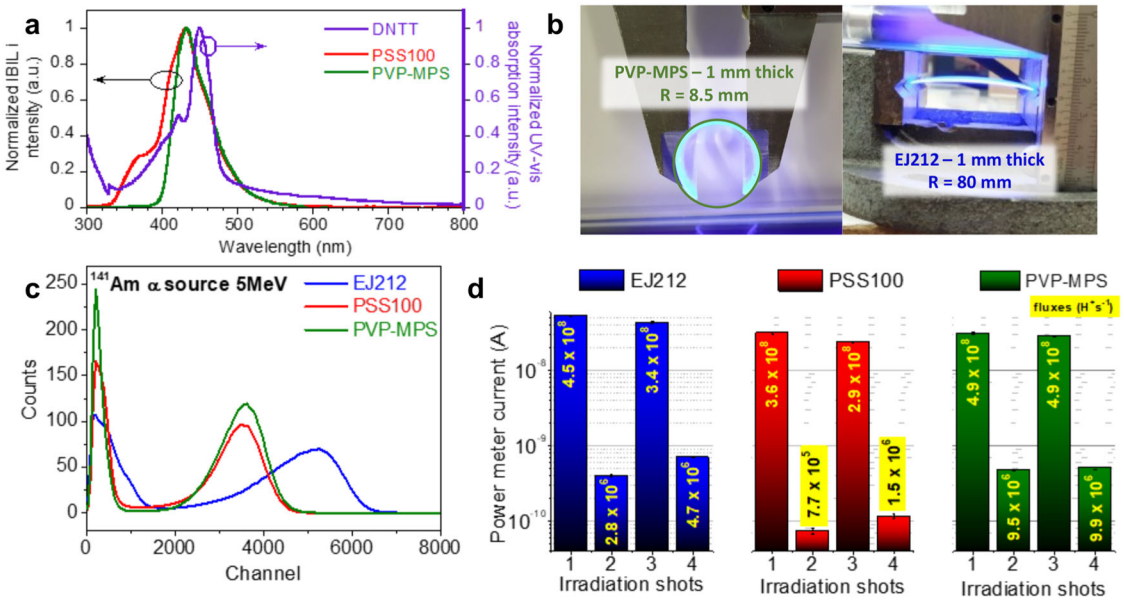

Fig. 2 Characterization of the plastic scintillator. a Normalized ion beam-induced luminescence (IBIL) spectra of scintillators based on PSS100 and PVP-MPS matrices, collected at fluences of about 5×10^8 $H^+ s^{-1}$ at 2 MeV (left axes, the experimental setup is reported in Supplementary Fig. 3). Comparison with the UV–vis absorbance spectrum of the DNTT (right axes). **b** Pictures of PVP-MPS siloxane scintillator (left) and commercial EJ-212 (right) under different bending conditions: the elastic siloxane undergoes severe deformation without cracking under negligible applied stress, whereas the EJ-212 of the same thickness must be strained in an iron grip to achieve a barely visible curvature. The reader can refer to Supplementary Table 2 for further information on the base matrix features. **c** Scintillation pulse height spectra of PSS100 (red line) and PVP-MPS (green line) scintillators. The spectrum of EJ212 (blue line) is shown for comparison. **d** Response measured with a power meter of the different scintillators at repeated shots in the same spot with alternating high and low 5 MeV proton beam fluxes, as indicated in correspondence of the bars. The values measured for EJ-212 are also shown for comparison.

source (emitting 5.443 MeV alpha particles) as compared with EJ-212 commercial scintillator with the same thickness. Siloxane-based scintillators display optimal light output, with values around 70% of the benchmark scintillator.

To assess the reliability of PSS100 and PVP-MPS scintillators under high fluxes of charged particles, their light emission was recorded and compared with a standard EJ-212 scintillator, as a current variation of a power meter during irradiation with alternated high and low proton beam fluxes, fixing the irradiation time to 10 s (Fig. 2d). The output is negligibly affected by consecutive shots on the same spot, irrespectively of the intensity of beam flux, and the measurement results highly repeatable, as for the same beam flux the same output current is measured. The almost constant response in terms of emitted power, irrespectively of the total received dose, which has been estimated as 0.02 Gy (low) and 20 Gy (high), proves that the siloxane base polymer is almost inert to the deposited energy. Further, it testifies that the bond strength of the Si–O–Si unit guarantees the collection of a reliable and stable signal, in the range of total proton doses here applied, i.e., much higher than the ones expected for an effective proton therapy treatment plan. These results indicate that the response of PSS100 and PVP-MPS scintillators is reliable and stable, showing no evident radiation damage effects in light emission.

OPT performance

The configuration of the developed OPT is staggered bottom gate top contact (Fig. 3a) realized onto a flexible substrate (Fig. 3b). Typical transfer characteristics in dark and air environments are reported in Fig. 3c. These do not highlight any hysteretic behavior in forward and reverse scans. The devices have threshold voltage (V_{TH}) around −13 V, onset voltage ranging from −6 to 3 V, subthreshold slope down to 1.8 V dec^{-1} and the $\log(I_{ON}/I_{OFF})$ is between 5 and 6 high (transistor figures of merit are calculated according to[35,36]). Gate leakage current is $I_{gs} < 10$ nA at $V_g = -30$ V. The OPT field effect mobility in linear regime is $\mu_{FE} = (1.1 \pm 0.2)$ $cm^2 V^{-1} s^{-1}$, this value is in class with the highest mobility for polycrystalline DNTT-based transistors on rigid substrates[37–40]. The low variability, combined with a device yield as high as 100%, confirms the high reproducibility of the OPT performance.

A relevant feature to be considered is the stability under bias stress, which is necessary to discriminate light and gate bias effects, to ensure enduring performance reliability, and to measure a significant photocurrent even at very weak light intensities due to the absence of compensation effects between the two mechanisms[41,42]. The devices have shown high stability, as previously reported[43], with maximum variation $\Delta V_{TH} \approx 260$ mV after stress time and biases higher than those in the expected operating conditions (Supplementary Fig. 6a), without significant mobility variation ($\Delta\mu_{FE}$, = 0.4%).

The OPTs were tested under repeated bending cycles, as reported in Fig. 3c, showing no relevant hysteresis or variation in μ_{FE}. Such results are significantly improved compared to the degradation reported for conformable phototransistors[44,45].

A spin-coated fluoropolymeric film was used as an encapsulation layer, able to protect the active layer from environment[43,46], prevent damage to the OPT during the coupling with the scintillator, and offer a suitable adhesion interface, transparent to the wavelengths of the scintillator light. Adhesion features were confirmed experimentally (Fig. 1b and Supplementary Fig. 5), and the required optical properties are ensured by the polymer high light transmittance ratio and internal transmittance (95% and > 99%, respectively). The efficacy of such an encapsulation layer for the OPT/scintillator coupling is confirmed by the good overlapping of the OPT transfer curves recorded before and after the coupling step (Supplementary Fig. 6b).

The dynamic photoresponse of the OPT was characterized under irradiation at 460 nm light pulses at different irradiances (Fig. 3d). A light pulse width of 10 s has been chosen to emulate

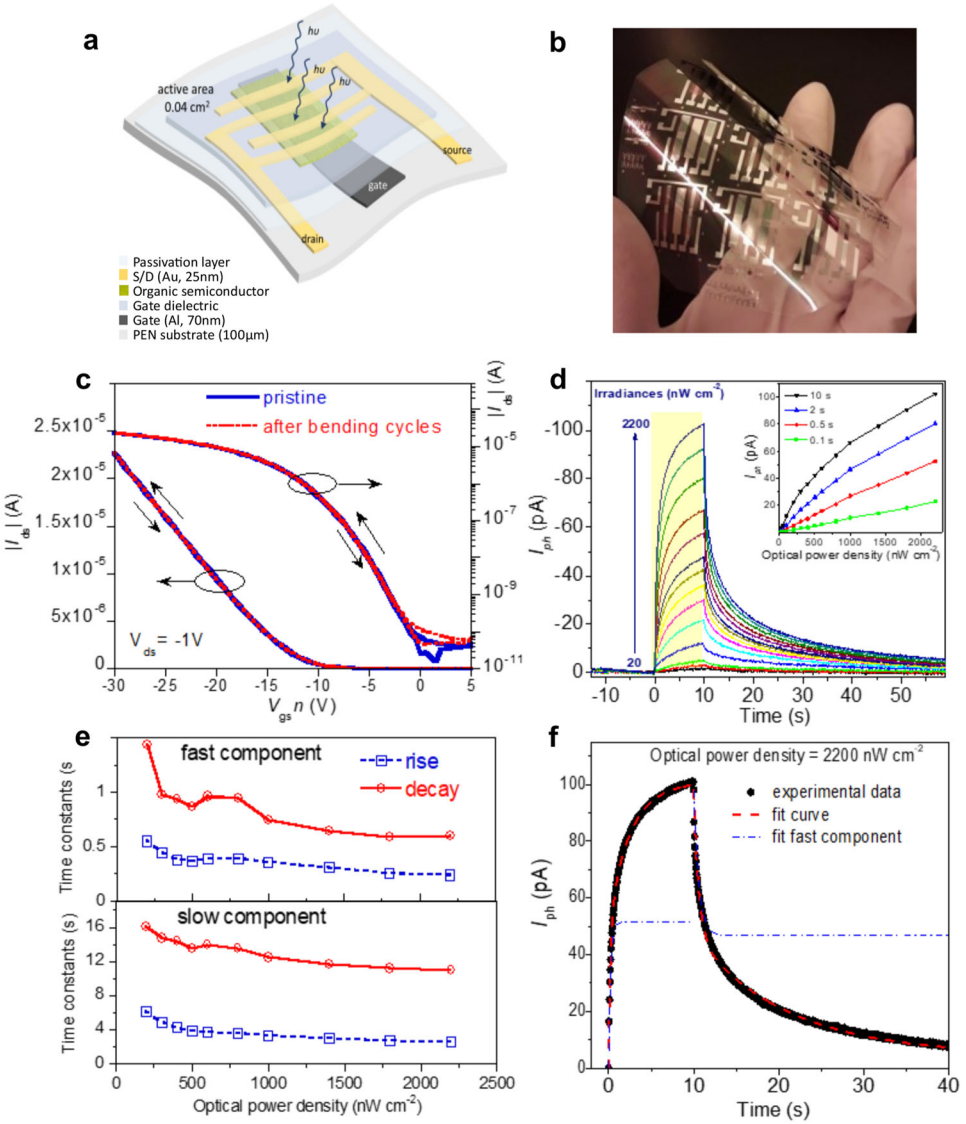

Fig. 3 Characterization of the organic phototransistor. a Phototransistor scheme (out of scale). **b** Sample picture. **c** Typical transfer characteristics of the device before and after 100 cycles of strain bending perpendicular to the channel. Forward and reverse curves are reported, as indicated by the up/down arrows. **d** Dynamic photoresponse of the OPT under different irradiations at $\lambda = 460$ nm. Exposition time $t_{exp} = 10$ s, $V_{ds} = -1$ V, $V_{gs} = -3.5$ V. In the inset, the photocurrent is reported as a function of the optical power for different exposition times. **e** Characteristic τ of the signal formation and decay as a function of the pulse optical intensity. **f** OPT photoresponse to a 2200 nW cm^{-2} light pulse with superimposed the fitted curve (red dashed line). Details of the fast component contribution to the formation and decay (blue line) processes are also shown.

the operating conditions used during the measurements under proton beam irradiation, which fits the lowest exposure times of protontherapy treatments[47,48]. The increase of the drain current (I_{ds}) is defined as photocurrent $I_{ph} = I_{ds,light} - I_{ds,dark}$, where $I_{ds,dark}$ is the I_{ds} before illumination and $I_{ds,light}$ is the I_{ds} under light exposure. A good linearity is observed for pulse width up to 0.5 s while, for longer exposure times, the response of the organic semiconductor to visible light shows an increasing non-linearity at high irradiances (see the inset of Fig. 3d), a feature that is well recognized in literature[32].

The lowest detectable optical power density in these experimental conditions, also known as the limit of detection (*LoD*), was evaluated following the IUPAC definition[49], as the minimum radiation flux that provides the signal-to-noise ratio of 3 (SNR = 3). The *LoD* value was obtained from a linear fit of the photoresponse curve for pulse widths of 10 s in a low optical power density range, as $LoD = 3\sigma/\text{slope}$, where σ is the noise floor of the setup (Supplementary Fig. 7). The estimated value is ≈18.5 nW cm^{-2}.

In order to quantify the time performances of the OPT response under pulsed illumination, both formation and decay of the I_{ph} vs. time waveforms were fitted with the equations:

$$I_{ph}^{formation}(t) = A_1(1 - \exp(-t/\tau_1)) + A_2(1 - \exp(-t/\tau_2)) \quad (1)$$

$$I_{ph}^{decay}(t) = A_3 \exp(-t/\tau_3) + A_4 \exp(-t/\tau_4) \quad (2)$$

where A_i is the amplitudes of exponential functions, and τ_i are the pertaining time constants. According to[50–52], the use of two-time constants allows an accurate reproduction of the photocurrent dynamics in the time range considered (20 s), corresponding to the largest I_{ph} variation, and permits quantifying the detector response-time performance. The fits clearly show a fast and a slow component (Fig. 3e). In the pulse formation, the fast component has time constants from about half a second to a few tenths of seconds,

whereas the slow component ranges from about 6 s to a few seconds. During the pulse decay, the fast component time constants range from about 16 s to nearly 10 s, while the slow one spans from about 1.5 s to about 0.5 s. For both components, the time constants decrease with the pulse optical power. Figure 3f shows the OPT photoresponse at 2200 nW cm^{-2} with superimposed fitted curve according to Eq. 1 and Eq. 2. The figure also shows the detail of the fast component contribution to the formation and decay process. For optical power higher than 1 μW cm^{-2} nearly half of the pulse swing is due to the fast components, both during formation and decay. Such behavior makes it possible to deploy this OPT as a detector in practical applications requiring a bandwidth in the order of Hz.

Characterization of integrated fully organic indirect proton detector

Fully organic coupled indirect detectors were tested under cycles of exposures to a 5 MeV proton beam, with fluxes of particles in the range of $(10^6 \div 10^{10})$ H$^+$ s^{-1} cm^{-2}, employing the experimental setup reported in the 'Methods' section. The exposure time was kept constant at 10 s. During irradiation, the OPT was polarized in a subthreshold regime, slightly above the onset ($V_{ds} = V_{gs} = -1$ V), to achieve the best compromise between responsivity and photosensitivity of the sensor[43]. The dynamic response of the detector to the different proton fluxes is reported in Fig. 4a, where the yellowish area indicates the proton irradiation window. The photocurrent shows a steep increase upon irradiation and follows the typical OPT response dynamics reported in Fig. 3d, assessing the effective coupling between the scintillating film and the underlying OPT fabricated on a plastic substrate. Figure 4b reports the photocurrent values normalized to the dark current (i.e., the current flowing within the OPT channel in the absence of proton irradiation) as a function of the impinging proton flux, recorded with detectors employing the two proposed scintillator films: PSS100 and PVP-MPS. In both cases, the sensor response results proportional to the proton flux and, as expected from the scintillation pulse height spectra under alpha particle irradiation reported in Fig. 2c, the signal amplitudes are comparable for both scintillators at the same proton flux. The *LoD* values of the here reported full organic indirect proton detectors are as low as 3.4×10^4 H$^+$ cm^{-2} s^{-1} (0.043 Gy min^{-1}) and 1.9×10^4 H$^+$ cm^{-2} s^{-1} (0.026 Gy min^{-1}) for PSS100 and PVP-MPS, respectively (Supplementary Fig. 8). These values are well in line with the proton rate required for our target application, the excessive dose detection in prostate cancer proton therapy, which is typically $(0.012 \div 0.07)$ Gy min^{-1}. In the Supplementary Information section, Supplementary Table 3 reports the comparison of the operative ranges of the most recent proton detector reported in the literature to the best of the authors' knowledge.

The bendability of the whole detector (i.e., scintillator coupled with the OPT on the flexible substrate), was assessed under proton flux on two detectors with almost identical OPT transfer characteristics, one kept in a flat configuration and the other bent at a radius of 0.5 cm (Supplementary Fig. 9), a value chosen to be conformable to most of the human body curves in view of possible medical dosimetry applications. The comparison of the proton-induced photocurrent for flat and bent samples as a function of the impinging proton flux is shown in Fig. 4c. The detectors exhibit comparable performance when exposed to similar proton fluxes in the range $(2 \times 10^7 \div 4 \times 10^8)$ H$^+$ s^{-1}, with slightly higher values (about 15%) of proton induced photocurrent for the bent device. Additional characterization of the unvaried detector response at different bending radii, upon optically exciting the scintillator, is reported in Supplementary Fig. 10. Similar behavior was reported for organic-based flexible direct detectors under X-ray exposure, with an even higher deviation of bent device response from flat condition[8,53]. To further evaluate the stability of the operation of the detectors, their tolerance to high proton irradiation up to 3×10^{10} H$^+$ was tested, resulting in almost unvaried OPT transfer characteristics (Fig. 4d), with a moderate increase of the off current due to the long recovery time of the OPT response to UV-Vis light emitted by the scintillator, as will be discussed in detail in the next section. The detector exhibits high stability of the response under 6.5×10^7 H$^+$s^{-1} cm^{-2} (56.7 Gy min^{-1}) pulsed irradiation, as reported in Fig. 2d. The time response of full detectors under proton irradiation was analyzed by using Eq. 1 and Eq. 2. In the range of proton fluxes used in these tests, the time constants have comparable values to the ones obtained under direct UV–vis photons exposure (Fig. 4e).

In order to assess a method able to predict the OPT performance in the indirect detector configuration starting from the optical response, the response of the OPT under light and of the full detector under protons were compared. In Fig. 4f the optical power density produced under proton irradiation by PSS100 and PVP-MPS scintillators and the optical power densities needed to generate the experimentally observed I_{ph}, as derived from the $\lambda = 460$ nm LED stimulus, are shown. The light power generated by the scintillator when irradiated with protons (same energy and flux as in the previous tests) was measured by directly coupling it to a calibrated power meter. The resulting photo-response trends are clearly parallel, and the observed shift could be ascribed to two main systematic effects: (i) LED and scintillator-emitted lights have different spectral distributions, and optical coupling with the OPT; (ii) the actual size of the light spots produced by the LED and by the scintillator is not identical. On such a basis, the two photo-response data sets could be considered in reasonable agreement and allow our setup to predict the trend of the whole detector response to the proton beam, starting from the OPT optical characterization.

Kinetic model

Photocurrent in organic semiconductors has been related by several authors to an increase of trapping of minority carriers induced by light exposure[8,54–57]. The measurements reported in this work for the OPTs are consistent with this interpretation. As shown in Fig. 4d, the electrical transfer characteristics of the OPT in the detector, measured before and after exposition to a proton flux, show a $I_{ph}/I_{ds,dark}$ that is maximum in low V_{gs} operation (subthreshold and off-regime). The corresponding current variations that are observed in our devices can be reproduced (Supplementary Fig. 11a) by a field-effect 1D simulation[58,59] introducing, as a consequence of light exposure, a deep trapping acceptor level in the HOMO–LUMO energy gap, located at 0.4 eV from the HOMO level. We note that light-induced creation of deep traps for charge carriers in the energy range $(0.3 \div 0.7)$ eV from HOMO level has already been evidenced experimentally in the analysis of several organic semiconductors used in different optoelectronic applications[60–62]. Moreover, 1D simulations, for the range of visible radiation exposures (on OPTs) and proton beam exposures (on detectors) used in this work, show that the photocurrent can be assumed linearly dependent upon the total amount of generated traps $N(t)$:

$$I_{ph}(t) = c_I N(t) \tag{3}$$

where the proportionality factor $c_I = \partial I_{ph}/\partial N$ depends on the specific polarization used for the OPT (see Supplementary Fig. 11b for an estimation at $V_{gs} = V_{ds} = -1$ V). Several microscopic mechanisms have been proposed to account for a photo-induced increase of deep traps, and, among the others, the creation of structural defects by photo-oxidation[63], cross-linking[64] and hydrogen abstraction (migration)[65]. The precise identification of the microscopic mechanism responsible for the photocurrent behavior is out of the scope of this work, nonetheless, it is important to develop a dedicated kinetic model able to properly describe the photocurrent behavior in our device to gain a better understanding and control of their application as proton detectors.

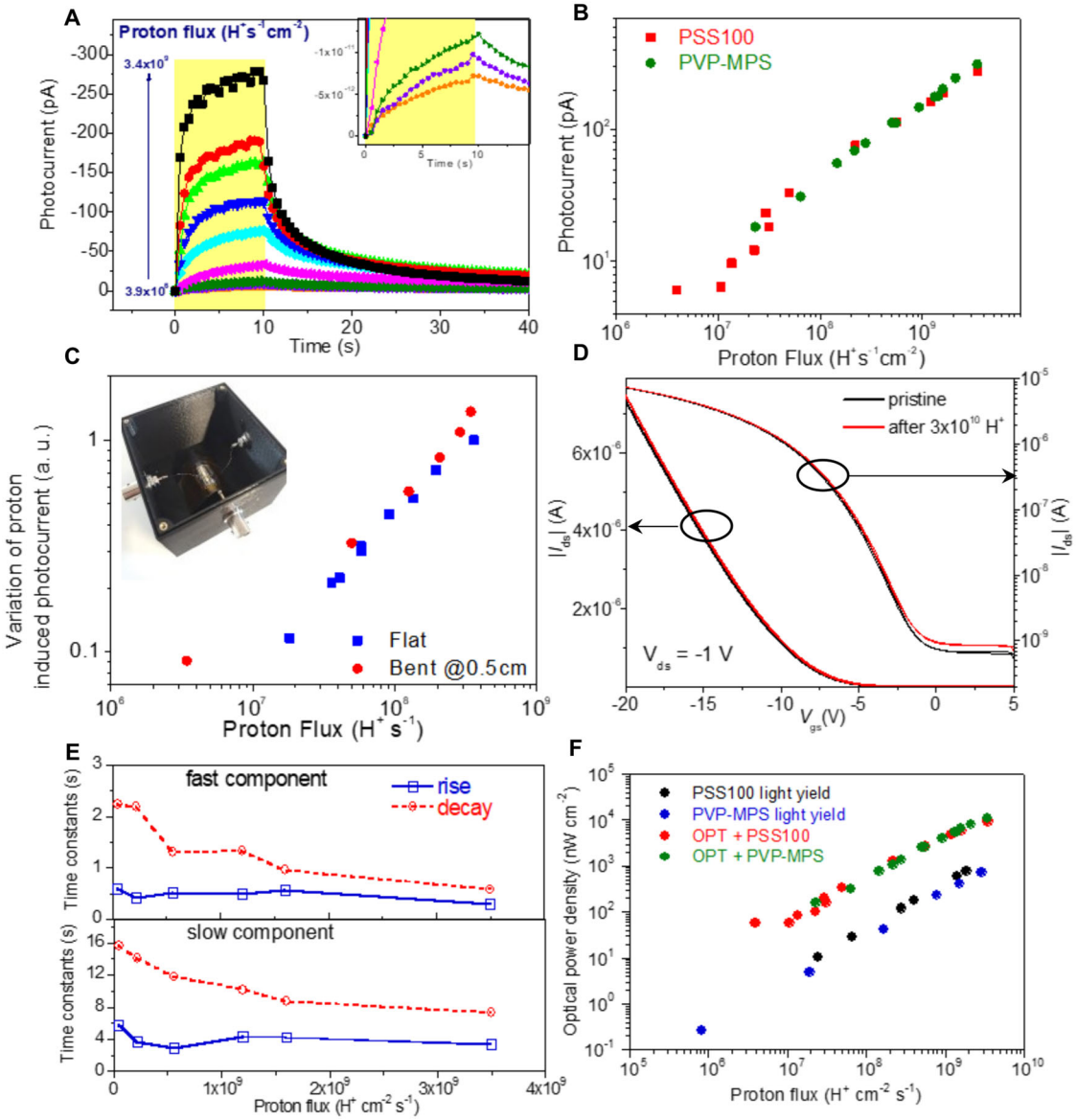

Fig. 4 Proton detection response of fully organic flexible indirect detectors. a Dynamic response of a detector with a PSS100-based scintillator for different impinging proton fluxes. The inset expands the lower fluxes. Exposure time window: $t_{exp} = 10$ s; OPT working polarization: $V_{ds} = V_g = -1$ V. **b** Values of the photocurrent normalized to the dark current as a function of the proton flux (red squares for PSS100 and green circles for PVP-MPS scintillators). $t_{exp} = 10$ s. **c** Variation of proton-induced photocurrent normalized by the maximum value recorded for the detector in flat configuration vs. the proton flux impinging onto the device, for the flat (blue squares) and the bent (red circles) samples. The inset shows the experimental set-up used for the characterization of the detector during bending. **d** Typical transfer curves of the detector with PVP-MPS-based scintillator before and after exposure under irradiation at 6.5×10^7 H^+ s^{-1} cm^{-2} for $t_{exp} = 50$ min. Forward and reverse curves are reported. **e** Characteristic τ of the signal formation and decay as a function of the proton flux. **f** Optical power density generated by the stand-alone scintillators (black and blue dots) as a function of the proton flux and by the indirect detector (OPT coupled with the scintillator) under proton irradiation (red and green dots) expressed in terms of equivalent optical power density as a function of the proton flux.

The dynamic photocurrent measurements on our organic devices (Fig. 5a, b, experimental curves) show two distinctive features:

(1) The relaxation in the dark of the photocurrent is well described by a stretched exponential (Supplementary Fig. 12a) with an exponent β almost constant (around 0.5), and a characteristic time τ_s that strongly depends on the exposure conditions ranging in the interval $(2 \div 8)$ s (Supplementary Fig. 12b). This kind of dynamical response has been already evidenced in different organic- and inorganic-based devices[8,43,66] supporting the presence of a distribution of activation energies for the recovery of trapping centers often related to the lack of crystallinity of the semiconductor thin-film. By applying the theory described in[67], these values of τ_s and β can be associated with the presence of defects with recovery activation energies distributed as a gaussian with an expected value $\varepsilon_1 \approx 0.7$ eV and a variance of $\delta_1 \approx 50$ meV. We note that a stretched exponential behavior can be effectively reproduced, on short time intervals, by a superposition of a few exponentially decaying components, thus confirming the validity of the approach adopted in the section 'OPT performance' to characterize the dynamic performances of the detector on short time ranges.

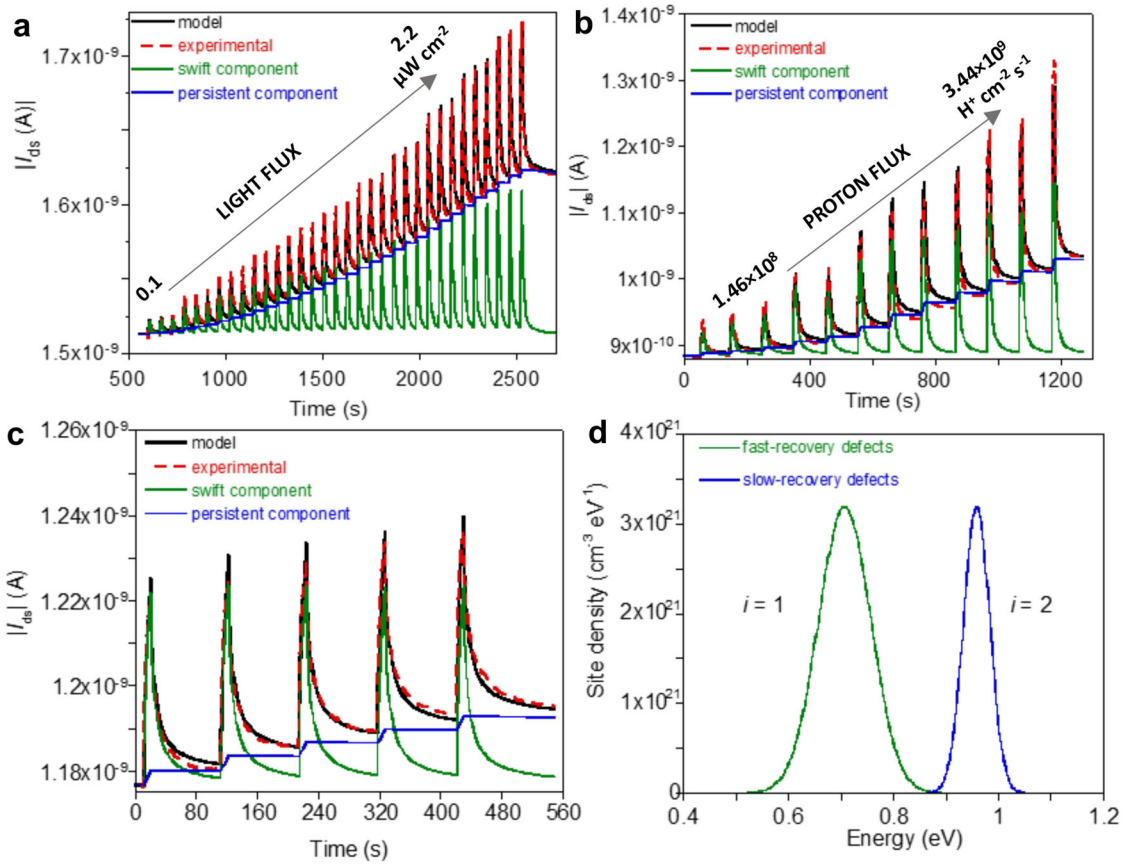

Fig. 5 Physical modeling of fully organic indirect proton detector. a Dynamic photocurrent measured (red line) and fitted (black line) of an OPT under light exposure (light pulses 10 s long, flux ranging from 0.1 μW cm^{-2} to 2.2 μW cm^{-2}); **b** fully integrated detector (PVP-MPS-based scintillator coupled to an OPT) under proton irradiation (beam pulses 10 s long and flux ranging from 1.46×10^8 H^+ cm^{-2} s^{-1} to 3.44×10^9 H^+ cm^{-2} s^{-1}); **c** detector (PVP-MPS-based) under proton irradiation (repeated beam pulses 10 s long and flux equal to $(7 \div 8) \times 10^7$ H^+ cm^{-2} s^{-1}). In panels (**a**–**c**) are also shown the two components, swift (green lines) and persistent (blue lines), of the photocurrent. The increase of the current baseline in (**c**) is around 3.6 pA after each exposure. **d** Energy density distributions of sites that can host fast- (green line) or slow-recovery (blue line) defects.

(2) Dynamic photocurrent measurements under repeated exposures show a systematic drift due to the buildup of a persistent component of the photocurrent[54,55,68]. The resulting dark current increase is clearly noticeable in the measurements made on the OPT under light exposure (Fig. 5a) as well as in the measurements on the detector under proton irradiation (Fig. 5b, c). The persistent photocurrent component has a recovery time of the order of 10^5 s (more than one day in the dark), which is much longer than the characteristic time τ_s of the swift component discussed above. It must be associated with defects with a distribution of activation energies with a mean value ε_2 considerably higher than ε_1.

The above experimental evidence suggests that there are at least two kinds of photo-induced defects determining the photoresponse: both have distributed recovery activation energies, in order to account for the stretched exponential behavior, but the mean values of these distributions must be different, as they relate to the swift and the persistent photocurrent components, respectively. To model these effects, the rate equation proposed by Street et al.[60] was modified by introducing two kinds of defects, instead of only one, with distributed recovery activation energies, instead of a fixed value (see Fig. 5d).

The proposed model (described in detail in Supplementary Information, Note 5) is able to quantitatively reproduce the dynamical photoresponse for a wide range of exposure intensities under both photon and proton fluxes. As seen in Fig. 5a–c, the curves computed by the model with the fitted parameters nicely superimpose the experimental ones, correctly reproducing the rise and fall dynamic of the exposure-response and the progressive build-up of a persistent photocurrent. The swift and persistent contributions to the photocurrent given by the fast- and slow-recovery defects, respectively, are also reported in the three panels. The slow-recovery defects determine a relatively small increase of the photocurrent during the exposure phase that, on the time scales of Fig. 5, does not recover appreciably during the dark phase, thus determining the systematic drift of the photocurrent baseline. On the other hand, it is apparent that the fast-recovery states give the bigger contribution to the photocurrent variation during the exposure, and they recover almost completely in a few tens of seconds during the dark. Hence, the slow recovery time of the persistent component does not affect the reproducibility of the device response for pulsed low light intensities, as shown in Fig. 5c and already reported for the phototransistor elsewhere[43].

The model gives also some valuable physical insight in explaining some features of the dynamical photoresponse. In particular, the reduction of the characteristic fall time τ_s with increasing fluxes (Supplementary Fig. 12b) is well reproduced and can be related to the shift of the steady state distribution of the defect activation energies towards lower values as the flux values are increased.

DISCUSSION

The herein presented results demonstrate a bendable indirect fully organic proton detector able to quantitatively monitor in real-time the dose released by MeV proton beam irradiation. The detector was developed for this application, testing the device in order to assess its reliability for the excessive dose monitoring in MeV proton therapy, but the versatility of the organic materials and of the adopted device architecture used allows us to easily tune its properties for other applications. The scintillator emission wavelength properly matches the optical absorption of the OPT active layer. The herein proposed PSS100 and PVP-MPS-based scintillating films present an optimal combination of mechanical and optical properties, and their response under proton exposure is reliable and stable, not showing degradation in light emission nor other evident radiation damage effects. The light response of both formulations is quite similar, and the variation in reactive vinyl group concentration does not affect the radiation resistance, in the adopted experimental conditions. The developed OPTs have high field-effect mobility, $\mu_{FE} = (1.1 \pm 0.2)\ cm^2\ V^{-1}\ s^{-1}$, and high stability under bias stress. The transistors were proved to be suitable for flexible applications, being unaffected by repeated bending cycles. The encapsulation layer efficiently protects the active layer from the environment and aging, while granting an efficient coupling with the scintillator.

The full device shows response stability and reproducibility under pulsed proton flux, in the typical operating conditions of a proton therapy session. We detect a minimum dose rate down to $0.043\ Gy\ min^{-1}$ and $0.026\ Gy\ min^{-1}$, respectively, for the OPT coupled with PSS100 and PVP-MPS-based scintillators. The detector response trend is unaffected by bending stress and the proton-induced photocurrent shows only a slight increase in bent devices. The detector operates at a very low bias voltage ($V_{ds} = V_{gs} = -1\ V$), hence it is compliant with basic safety constraints for electrical hazards and with a low power supply.

The kinetic model presented here allows getting a proper physical insight into the detector response mechanism. The model is able to quantitatively reproduce the dynamic response of the detector under proton irradiation, which was compared with the behavior of the OPT under UV–vis light. The computed curves nicely superimposed the experimental ones for both conditions, confirming that the OPT response is entirely due to the effect of the light emitted by the scintillator, as expected by the proton penetration depth calculated through SRIM simulations to terminate within the scintillator. The response in the operating range of the detector, the rise and fall dynamic, and the progressive build-up of a persistent photocurrent are correctly reproduced. The two components identified in the response under proton flux (a swift and a persistent one) were attributed to two kinds of photo-induced defects with different mean values of the distribution of the recovery activation energies. It was demonstrated experimentally and confirmed by the computational analysis that the fast response is recurring, independently from the persistent current drift, thus assessing the suitability of the here proposed devices as a real-time proton detector. Finally, the quantification of the two components in the detector response can be exploited to operate in two simultaneous modes, as recently proposed for direct organic proton detectors with a similar behavior[69]: (i) the real-time monitoring of proton irradiation and (ii) the monitoring of the total received dose.

This work demonstrates the potential of fully organic thin-film flexible devices for a variety of applications within the proton detection field, from experimental scientific research to innovative theranostics.

METHODS

Proton irradiation and detection tests

The detectors were characterized using a 5 MeV proton beam provided by the 3 MV Tandetron accelerator of the LABEC ion beam center (INFN Firenze, Italy)[70]. The beam is extracted into ambient pressure through a 200-nm-thick Si_3N_4 membrane; the sample is typically installed at a distance of 8 mm from the extraction window. The proton beam current employed during the experiment was in the range $(0.03 \div 94)$ pA, corresponding to $(1.09 \times 10^6 \div 3.5 \times 10^9)\ H^+\ cm^{-2}\ s^{-1}$ proton fluxes. The intensity of the beam is monitored and measured by a rotating chopper[71], placed between the Si_3N_4 window and the sample, that intercepts the beam. The chopper is a graphite vane covered with thin nickel evaporation, and the Ni X-ray yield is used as an indirect measurement of the beam current. To determine the actual energy of the protons impinging onto the top siloxane scintillating layer, the energy lost by the protons passing through the several layers interposed between the beam and the sensor has to be calculated, including 200 nm of Si_3N_4 for the beam extraction window, 8 mm of mixed air–He (50–50%) atmosphere in the gap between the extraction window and the metal box, 14 μm of Al for the entrance window of the box, where the sensor was enclosed, and 14 mm of air inside the box. After passing through these layers, protons lose about 390 keV, as calculated with the SRIM Monte Carlo code[31] During proton irradiation tests, the electrical photoresponse of the devices was measured by using a Keithley 2614 SourceMeter, controlled by a custom-made Labview software. All measurements were carried out keeping the device in the dark, in a Faraday cage, to reduce electrical noise and avoid light-induced photogeneration in the organic semiconductor.

The measurement of the detector response under bending was performed by using a customized 3D printed box with a curved bottom in order to place the detector in the bent configuration, as shown in Supplementary Fig. 9c. The measurement of the detector's response in a flat configuration and at different bending radii upon optically exciting the scintillator reported in Supplementary Fig. 10 has been performed a Thorlabs SLS400 Xe lamp powered at 150 W coupled a SPEX 500 spectrometer.

Scintillator fabrication, characterization, and modeling

Polysiloxane scintillators were produced using vinyl-terminated polymethylphenyl-co-phenylvinyl siloxane or polymethylphenylsiloxane as starting resins (PVP-MPS and PMPS), which undergo vulcanization by Pt-catalyzed addition with a silane containing cross-linking resin as described elsewhere[72]. The structures of the base resins used herein and other peculiar features are reported in Supplementary Table 2.

After the addition of proper additives and cross-linker, the viscous precursor is cast in the form of 0.5 mm thin sheets, using a film applicator and a motorized stage (Erichsen, model Unicoater 509). The resin is spread over a glass plate, previously treated with a thin layer of Teepol, as a release agent. Then, the thin layer is left to dry and cross-link overnight at 60 °C, prior to easy detachment by immersion in water to produce a self-standing film, as shown in the photo of Supplementary Fig. 4.

To collect the IBIL spectra, the samples were irradiated with 2 MeV protons and beam current $(1 \div 2)$ nA at the AN2000 accelerator (INFN-LNL). The measurement is done into a vacuum chamber located along the beam line, and the sample is directly exposed to the beam, while an optical fiber is fixed at 45° with respect to the sample surface to collect scintillation light[73], as shown in Supplementary Fig. 3. An optical spectrometer is connected to the fiber through proper vacuum/air feedthrough and gathers one spectrum every 5 s during the irradiation, which lasts on the whole about 600 s The total charge is gathered by a Faraday cup and measured over the entire period of irradiation; then, the value of dose rate in ions/s can be derived as an average

value. The spectra herein reported are referred to the normalized scintillation intensity collected after the first 5 s irradiation.

The power meter used for the scintillation light measurement is a 818-SL by Newport.

The polysiloxane-based scintillating layer was applied on the top of the OPT device with a thin layer of optical cement EJ-500 (Eljen Technology), which assures a fast and robust bonding between the polysiloxane-based film and the Cytop™ passivation layer. After the application and adhesive curing, the bi-layer was bent to the required curvature radius and fixed on the curved support using Kapton tape, as shown in the photo of Supplementary Fig. 5.

OPT fabrication and characterization

The OPT fabrication details are reported in[43]. In brief, the process was carried out in a cleanroom environment at a low temperature, within 100 °C, directly on the free-standing plastic foil, a PEN (100 µm thick, Teonex® Q65FA, DuPont Teijin). The dielectric and encapsulation layers are a fluoropolymer-based material (Cytop™, AGC Chemicals), deposited by spin-coating, 600 nm and 240 nm thick, respectively. All the other layers were thermally evaporated through shadow masks (Stencils Unlimited). The gate is Al 70 nm thick, the semiconductor is dinaphtho[2,3-b:2′, 3′-f]thieno[3,2-b] thiophene (DNTT), 50 nm thick (assay 99%, as purchased, Merck), the source and drain (S/D) contacts, Au 30 nm thick, the connections and pads, Al 70 nm thick. The via-holes were obtained via plasma oxygen. Electrical characterization of the devices was carried out at room temperature in ambient environment, using a probe station equipped with two Keithley 236 source meter. The bending test setup is reported in[74]. The bending radius was 5 mm, the frequency 0.5 Hz, while the bending direction was chosen to be perpendicular to the channel length to test the device in the worst working conditions. The tests for the photoresponse at 460 nm were carried out by sending light pulses from a calibrated LED source, emitting at 460 nm (Broadcom). The LED driver allows spanning the optical power density range from nW cm^{-2} to a few µW cm^{-2}.

DATA AVAILABILITY

All data are available on request to the corresponding author.

Received: 2 August 2022; Accepted: 10 November 2022;
Published online: 06 February 2023

REFERENCES

1. Posar, J. A., Petasecca, M. & Griffith, M. J. A review of printable, flexible and tissue equivalent materials for ionizing radiation detection. *Flex. Print. Electron.* **6**, 043005 (2021).
2. Chen, M., Wang, C. & Hu, W. Organic photoelectric materials for X-ray and gamma ray detection: mechanism, material preparation and application. *J. Mater. Chem. C* **9**, 4709–4729 (2021).
3. Durante, M. & Loeffler, J. S. Charged particles in radiation oncology. *Nat. Rev. Clin. Oncol.* **7**, 37–43 (2010).
4. Cuaron, J. J. et al. Exponential increase in relative biological effectiveness along distal edge of a proton Bragg Peak as measured by deoxyribonucleic acid double-strand breaks. *Int. J. Radiat. Oncol. Biol. Phys.* **95**, 62–69 (2016).
5. Britten, R. A. et al. Variations in the RBE for cell killing along the depth-dose profile of a modulated proton therapy beam. *Radiat. Res.* **179**, 21–28 (2012).
6. Inaniwa, T., Kanematsu, N., Noda, K. & Kamada, T. Treatment planning of intensity modulated composite particle therapy with dose and linear energy transfer optimization. *Phys. Med. Biol.* **62**, 5180–5197 (2017).
7. Hoesl, M. et al. Clinical commissioning of an in vivo range verification system for prostate cancer treatment with anterior and anterior oblique proton beams. *Phys. Med. Biol.* **61**, 3049–3062 (2016).
8. Basiricò, L. et al. Direct X-ray photoconversion in flexible organic thin film devices operated below 1 V. *Nat. Commun.* **7**, 13063 (2016).
9. Ciavatti, A. et al. Boosting direct X-ray detection in organic thin films by small molecules tailoring. *Adv. Func. Mater.* **29**, 1806119 (2019).
10. Nanayakkara, M. P. A. et al. Ultra-low dark current organic–inorganic hybrid X-ray detectors. *Adv. Funct. Mater.* **31**, 2008482 (2021).
11. Chatzispyroglou, P., Keddie, J. L. & Sellin, P. J. Boron-loaded polymeric sensor for the direct detection of thermal neutrons. *ACS Appl. Mater. Interfaces* **12**, 33050–33057 (2020).
12. Temiño, I. et al. Morphology and mobility as tools to control and unprecedentedly enhance X-ray sensitivity in organic thin-films. *Nat. Commun.* **11**, 2136 (2020).
13. Ciavatti, A. et al. Dynamics of direct X-ray detection processes in high-Z Bi2O3 nanoparticles-loaded PFO polymer-based diodes. *Appl. Phys. Lett.* **111**, 183301 (2017).
14. Fraboni, B., Fraleoni-Morgera, A. & Zaitseva, N. Ionizing radiation detectors based on solution-grown organic single crystals. *Adv. Func. Mater.* **26**, 2276–2291 (2016).
15. Carman, L. et al. Solution-grown rubrene crystals as radiation detecting devices. *IEEE Trans. Nucl. Sci.* **64**, 781–788 (2017).
16. Zhao, D. et al. Direct detection of fast neutrons by organic semiconducting single crystal detectors. *Adv. Func. Mater.* **32**, 2108857 (2022).
17. Ciavatti, A., Sellin, P. J., Basiricò, L., Fraleoni-Morgera, A. & Fraboni, B. Charged-particle spectroscopy in organic semiconducting single crystals. *Appl. Phys. Lett.* **108**, 153301 (2016).
18. Ciavatti, A. et al. Toward low-voltage and bendable X-ray direct detectors based on organic semiconducting single crystals. *Adv. Mater.* **27**, 7213–7220 (2015).
19. Posar, J. A. et al. Characterization of a plastic dosimeter based on organic semiconductor photodiodes and scintillator. *Phys. Imaging Radiat. Oncol.* **14**, 48–52 (2020).
20. Harmon, J., Gaynor, J., Feygelman, V. & Walker, J. Linear polydiorganosiloxanes as plastic bases for radiation hard scintillators. *Nucl. Instrum. Methods Phys. Res. B* **53**, 309–314 (1991).
21. Quaranta, A. et al. Characterization of polysiloxane organic scintillators produced with different phenyl containing blends. *Mater. Chem. Phys.* **137**, 951–958 (2013).
22. Carturan, S. M. & Quaranta, A. In *Plastic Scintillators: Chemistry and Applications* (ed Hamel, M.) 169–199, https://doi.org/10.1007/978-3-030-73488-6_5 (Springer International Publishing, 2021).
23. van Eijk, C. W. E. Inorganic scintillators in medical imaging. *Phys. Med. Biol.* **47**, R85–R106 (2002).
24. Natali, D. & Sampietro, M. Detectors based on organic materials: status and perspectives. *Nucl. Instrum. Methods Phys. Res. B* **512**, 419–426 (2003).
25. Baeg, K.-J., Caironi, M. & Noh, Y.-Y. Toward printed integrated circuits based on unipolar or ambipolar polymer semiconductors. *Adv. Mater.* **25**, 4210–4244 (2013).
26. Büchele, P. et al. X-ray imaging with scintillator-sensitized hybrid organic photodetectors. *Nat. Photon* **9**, 843–848 (2015).
27. Xiang, L. et al. Flexible indirect x-ray detector enabled by organic photodiode and CsPbBr3 perovskite quantum dot scintillator. *Flex. Print. Electron.* **6**, 015008 (2021).
28. Oliveira, J. et al. Indirect X-ray detectors based on inkjet-printed photodetectors with a screen-printed scintillator layer. *ACS Appl. Mater. Interfaces* **10**, 12904–12912 (2018).
29. Dalla Palma, M. et al. Non-toxic liquid scintillators with high light output based on phenyl-substituted siloxanes. *Optical Mater.* **42**, 111–117 (2015).
30. Perl, J., Shin, J., Schumann, J., Faddegon, B. & Paganetti, H. TOPAS: an innovative proton Monte Carlo platform for research and clinical applications. *Med. Phys.* **39**, 6818–6837 (2012).
31. Ziegler, J. F., Ziegler, M. D. & Biersack, J. P. SRIM—The stopping and range of ions in matter (2010). *Nucl. Instrum. Methods Phys. Res B* **268**, 1818–1823 (2010).
32. Baeg, K.-J., Binda, M., Natali, D., Caironi, M. & Noh, Y.-Y. Organic light detectors: photodiodes and phototransistors. *Adv. Mater.* **25**, 4267–4295 (2013).
33. Shidachi, R. et al. Photocurrent amplification in bulk heterojunction organic phototransistors with different donor-acceptor ratio. *Phys. Status Solidi RRL* **4,** 1700400, 1–4 (2018).
34. Erdmann, E., Destéfanis, H. A., Abalos, R., Frontini, P. M. & Abraham, G. A. Transport properties and mechanical behavior of poly(methyl-phenylsiloxane) membranes as a function of methyl to phenyl groups ratio. *J. Appl. Polym. Sci.* **85**, 1624–1633 (2002).
35. Zaumseil, J. & Sirringhaus, H. Electron and ambipolar transport in organic field-effect transistors. *Chem. Rev.* **107**, 1296–1323 (2007).
36. Newman, C. R. et al. Introduction to organic thin film transistors and design of n-channel organic semiconductors. *Chem. Mater.* **16**, 4436–4451 (2004).
37. Panigrahi, D. & Dhar, A. Tuning dielectric-semiconductor interfacial properties in organic phototransistors for ultralow light detection. *Org. Electron.* **70**, 107–112 (2019).
38. Za'aba, N. K., Morrison, J. J. & Taylor, D. M. Effect of relative humidity and temperature on the stability of DNTT transistors: a density of states investigation. *Org. Electron.* **45**, 174–181 (2017).

39. Kraft, U. et al. Detailed analysis and contact properties of low-voltage organic thin- film transistors based on dinaphtho[2,3-b:20,30-f]thieno[3,2-b] thiophene (DNTT) and its didecyl and diphenyl derivatives. *Org. Electron.* **35**, 33–40 (2016).
40. Acharya, R. et al. Stability of organic thin-film transistors based on ultrathin films of dinaphtho[2, 3- b:2′,3′- f]thieno[3, 2- b]thiophene (DNTT). *J. Mater. Chem. C* **9**, 270–280 (2021).
41. Liguori, R., Sheets, W. C., Facchetti, A. & Rubino, A. Light- and bias-induced effects in pentacene-based thin film phototransistors with a photocurable polymer dielectric. *Org. Electron.* **28**, 147–154 (2016).
42. Debucquoy, M. et al. Correlation between bias stress instability and phototransistor operation of pentacene thin-film transistors. *Appl. Phys. Lett.* **91**, 103508 (2007).
43. Calvi, S. et al. Highly sensitive organic phototransistor for flexible optical detector arrays. *Org. Electron.* **102**, 106452 (2022).
44. Liu, M. et al. Ultrathin air-stable n-type organic phototransistor array for conformal optoelectronics. *Sci. Rep.* **8**, 16612 (2018).
45. Xu, H. et al. Flexible organic/inorganic hybrid near-infrared photoplethysmogram sensor for cardiovascular monitoring. *Adv. Mater.* **29**, 1700975 (2017).
46. Rapisarda, M. et al. Water stable organic thin film transistors (TFTs) made on flexible substrates. in *Nanotechnology (IEEE-NANO), 2015 IEEE 15th International Conference on* 1430–1433. http://ieeexplore.ieee.org/abstract/document/7388907/ (IEEE, 2015).
47. Alsanea, F., Therriault-Proulx, F., Sawakuchi, G. & Beddar, S. A real-time method to simultaneously measure linear energy transfer and dose for proton therapy using organic scintillators. *Med. Phys.* **45**, 1782–1789 (2018).
48. Magalhaes Martins, P. et al. Towards real-time PGS range monitoring in proton therapy of prostate cancer. *Sci. Rep.* **11**, 15331 (2021).
49. Thompson M., Ellison S. L. R. & Wood R. Harmonized guidelines for single-laboratory validation of methods of analysis. *Pure Appl. Chem*. **74**, 835–855 (2002).
50. Dey, A., Singh, A., Das, D. & Iyer, P. K. Photosensitive organic field effect transistors: the influence of ZnPc morphology and bilayer dielectrics for achieving a low operating voltage and low bias stress effect. *Phys. Chem. Chem. Phys.* **18**, 32602–32609 (2016).
51. Jin, Z., Gao, L., Zhou, Q. & Wang, J. High-performance flexible ultraviolet photoconductors based on solution-processed ultrathin ZnO/Au nanoparticle composite films. *Sci. Rep.* **4**, 4268 (2015).
52. Sun, Z. et al. Infrared photodetectors based on CVD-grown graphene and PbS quantum dots with ultrahigh responsivity. *Adv. Mater.* **24**, 5878–5883 (2012).
53. Nanayakkara, M. P. A. et al. Molecular weight tuning of organic semiconductors for curved organic–inorganic hybrid X-ray detectors. *Adv. Sci.* **9**, 2101746 (2022).
54. Jia, R. et al. Unraveling the mechanism of the persistent photoconductivity in organic phototransistors. *Adv. Funct. Mater.* **29**, 1905657 (2019).
55. Singh, S. & Mohapatra, Y. N. Persistent photocurrent (PPC) in solution-processed organic thin film transistors: mechanisms of gate voltage control. *J. Appl. Phys.* **120**, 045501 (2016).
56. Za'aba, N. K. & Taylor, D. M. Photo-induced effects in organic thin film transistors based on dinaphtho [2,3-b:2′,3′-f] Thieno[3,2-b′] thiophene (DNTT). 65, 39–48 (2019). *Org. Electron.* **65**, 39–48 (2019)..
57. Liguori, R. & Rubino, A. Metastable light induced effects in pentacene. *Org. Electron.* **15**, 1928–1935 (2014).
58. Cipolloni, S. et al. Aging effects and electrical stability in pentacene thin film transistors. *Thin Solid Films* **515**, 7546–7550 (2007).
59. Rapisarda, M., Simeone, D., Fortunato, G., Valletta, A. & Mariucci, L. Pentacene thin film transistors with (polytetrafluoroethylene) PTFE-like encapsulation layer. *Org. Electron.* **12**, 119–124 (2011).
60. Street, R. A., Yang, Y., Thompson, B. C. & McCulloch, I. Capacitance spectroscopy of light induced trap states in organic solar cells. *J. Phys. Chem. C* **120**, 22169–22178 (2016).
61. Kalb, W. L., Haas, S., Krellner, C., Mathis, T. & Batlogg, B. Trap density of states in small-molecule organic semiconductors: a quantitative comparison of thin-film transistors with single crystals. *Phys. Rev. B* **81**, 155315 (2010).
62. Gupta, S. K., Tripathi, D. C., Garg, A. & Pathak, S. K. Determination of defect states and surface photovoltage in PTB7:PC71BM based bulk heterojunction solar cells. *Sol. Energy Mater. Sol. Cells* **224**, 110994 (2021).
63. Sai, N., Leung, K., Zádor, J. & Henkelman, G. First principles study of photooxidation degradation mechanisms in P3HT for organic solar cells. *Phys. Chem. Chem. Phys.* **16**, 8092–8099 (2014).
64. Wantz, G., Derue, L., Dautel, O., Rivaton, A., Hudhomme, P. & Dagron-Lartigau, C. Stabilizing polymer-based bulk heterojunction solar cells via crosslinking: Stabilizing polymer-based bulk heterojunction. *Polym. Int.* **63**, 1346–1361 (2014).
65. Street, R. A., Northrup, J. E. & Krusor, B. S. Radiation induced recombination centers in organic solar cells. *Phys. Rev. B* **85**, 205211 (2012).
66. Luo, J. et al. Transient photoresponse in amorphous In-Ga-Zn-O thin films under stretched exponential analysis. *J. Appl. Phys.* **113**, 153709 (2013).
67. Edholm, O. & Blomberg, C. Stretched exponentials and barrier distributions. *Chem. Phys.* **252**, 221–225 (2000).
68. Lutsyk, P. et al. Long-lived persistent currents in poly(3-octylthiophene) thin film transistors. *Org. Electron.* **11,**, 490–497 (2010).
69. Fratelli, I. et al. Direct detection of 5-MeV protons by flexible organic thin-film devices. *Sci. Adv.* **7**, eabf4462 (2021).
70. Chiari, M. et al. LABEC, the INFN ion beam laboratory of nuclear techniques for environment and cultural heritage. *Eur. Phys. J.* **136**, 472 (2021).
71. Chiari, M., Migliori, A. & Mandò, P. A. Measurement of low currents in an external beam set-up. *Nucl. Instrum. Methods Phys. Res. B* **188**, 162–165 (2002).
72. Carturan, S. M. et al. Temperature effects on light yield and pulse shape discrimination capability of siloxane based scintillators. *Eur. Phys. J. C* **80**, 1057 (2020).
73. Quaranta, A., Salomon, J., Dran, J. C., Tonezzer, M., & Della Mea, G. Ion beam induced luminescence analysis of painting pigments. *Nucl. Instrum. Methods Phys. Res B* **254**, 289–294 (2007).
74. Rapisarda, M. et al. Fully-organic flexible tactile sensor for advanced robotic applications. In *Nanotechnology Materials and Devices Conference (NMDC), 2014 IEEE 9th* 45–48 at http://ieeexplore.ieee.org/abstract/document/6997418/ (IEEE, 2014).

ACKNOWLEDGEMENTS

This work has been funded by the Italian National Institute of Nuclear Physics—INFN—5th commission, under the FIRE (Flexible organic Ionizing Radiation dEtectors) project (2019–2022) (https://www.bo.infn.it/gruppo5/en/fire_en/).

AUTHOR CONTRIBUTIONS

S.C. and L.B. wrote the main draft of the paper; S.C., M.R., and L.M. designed the OPTs, conducted their fabrication, electrical characterization, and bending test of OPTs; S.M.C., F.P., S.M., and S.B. fabricated the scintillators; S.M.C., L.B., A.C., I.F., and M.Ch. coupled the full device and carried out the proton irradiation experiments and L.B., I.F., M.V., and F.P. carried out the collected data analyses; A.C. implemented the software for data acquisition during proton irradiation experiments; I.F. and O.C. performed the characterization of the detector's response under bending; A.V. developed the kinetic model; A.A., M.Ca., and P.D.M. characterized the phototransistor under light, carried out the double exponential fit and the Fig. 4f comparison; S.D.R. and L.T. assessed the deposition and fabrication control process; F.T. carried out the Fig. 1c, d Monte Carlo simulations; E.S., A.Q., and P.B. supervised the activities of each group; B.F. coordinated the project.

COMPETING INTERESTS

The authors declare no competing interests.

ADDITIONAL INFORMATION

Supplementary information The online version contains supplementary material available at https://doi.org/10.1038/s41528-022-00229-w.

Correspondence and requests for materials should be addressed to Laura Basiricò.

Reprints and permission information is available at http://www.nature.com/reprints

Publisher's note Springer Nature remains neutral with regard to jurisdictional claims in published maps and institutional affiliations.